Digitalized K+ Occupancy in the Nanocavity Holds and Releases Queues of K+ in a Channel

Takashi Sumikama and Shigetoshi Oiki*

Department of Molecular Physiology and Biophysics, Faculty of Medical Sciences, University of Fukui, Fukui 910-1193, Japan

S *Supporting Information*

ABSTRACT: The mechanisms of ion permeation through potassium channels have been extensively examined. Molecular dynamics (MD) simulations have demonstrated that rapidly permeating ions collide near the selectivity filter (*SF*) ("knock-on" mechanism), but this oversimplified mechanism is insufficient to account for the experimentally observed single-channel current amplitudes. Here, we analyzed the MD-simulated ion trajectories through a Kv1.2 potassium channel using an event-oriented analysis method, and surprisingly, we found that the nanocavity (*NC*) governs ion permeation in a digital fashion. The *NC* has a maximal diameter of 10 Å and stands between the intracellular bulk solution and the *SF*, which holds only up to one K+ during permeation. Accordingly, the K+ concentration in the intracellular solution is translated as a digitalized zero or one K+ in the *NC*. When the ion number in the *NC* is zero, the multiple ions in the *SF* are mostly immobilized. By contrast, when the number of ions in the *NC* is one, the structured water in the *NC* mediates the ion-occupied status to the queueing ions in the *SF*, and the ions then initiate a collective outward motion. Accordingly, the one ion in the *NC* serves as a catalytic intermediate for permeation, which quantitatively accounts for the experimentally obtained conductance−concentration relationships. We conclude that the ion movements are coherent across the entire pore.
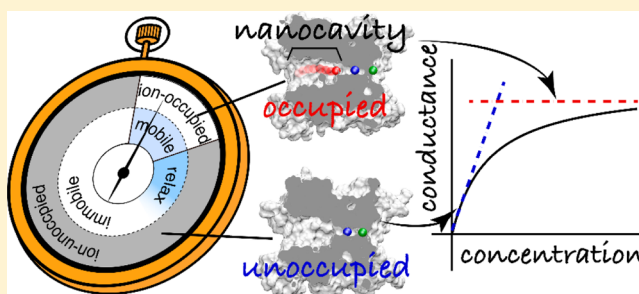
INTRODUCTION

The mechanism underlying the selective ion permeation of open gated potassium channels has been investigated in depth through both experimental and theoretical methods.[1−5] The elucidation of the crystal structure of the potassium channel yielded a clue in the investigation of the origin of its catalytic action or rapid ion permeation at the atomic level.[6] The permeation features have been further microscopically examined using molecular dynamics (MD) simulations, which have revealed the nature of the ion movements at the highest ever spatial and temporal resolution on the atomic spatial scale and the picosecond temporal scale.[7−15] In earlier studies, the simulations demonstrated a coupling of the entry of an ion into the selectivity filter (*SF*) and simultaneous exit of another ion from the *SF*, which is referred to as the knock-on mechanism.[16] These papers claimed that the knock-on process determines the permeation rate.[12,14,15] However, there are several concerns regarding this oversimplified view. Experimentally, the electrophysiologically measured currents have revealed that ion permeation through channels requires submicroseconds on average.[17] By contrast, the knock-on event elucidated from the MD simulations is a spatially localized event that requires only subnanoseconds.[9,12,15] Thus, the knock-on mechanism is at most a partial reaction in the permeation process that is insufficient to account for the entire ion permeation mechanism. Moreover, the single-channel current amplitudes through various types of K+ channels vary widely,[17−19] despite the highly conserved structure of the *SF*. These findings strongly

imply that parts other than the *SF* are critical for determining ion permeation rates.[20−22]

To understand the overall picture of permeation, we focused on the role of the water-filled nanocavity (*NC*). The *NC* is a tiny space that is frequently found in proteins in which anomalous and heterogeneous behaviors of molecules, especially ions, are expected, and its functional roles have generally been studied in protein structures.[23−25] In the K+ channels, the *NC* is more important because the permeating K+ must pass the *NC* before entering the *SF* (Figure 1A). Thus, the present work addresses the following simple question: What is the role of the *NC* in permeation? To capture the trajectories of ions throughout the entire pore (including both the *SF* and *NC*), we developed an event-oriented analysis method. In this analysis, a permeating ion undergoing an event, such as entering the *SF*, is the target of focus, and the temporal evolutions of the relevant ion and other ions are traced from the moment of the event. This method enabled us to directly visualize the correlated motions of the ions. Moreover, the temporal evolutions of the positional changes of each ion can be both anterogradely and retrogradely traced, which reveals the rate of ion movements.
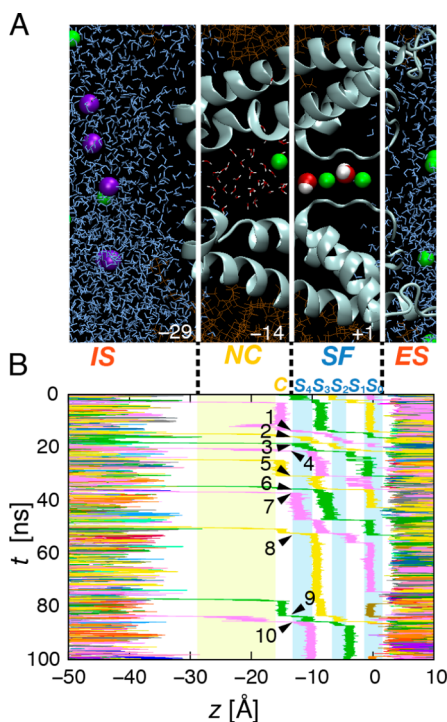
Figure 1. Structure of the Kv1.2 channel and the ion trajectories calculated in MD simulations. (A) Structure of the transmembrane pore domain of the Kv1.2 channel (cyan ribbon) in a membrane (brown line). Residues 322−409 in two diagonal subunits are shown. The permeation pathway from the intracellular space (IS) to the extracellular space (ES) is labeled; the nanocavity (NC) next to IS is followed by the selectivity filter (SF). There are five ion-binding sites in the SF, termed $S_4 - S_0$. K^+ and Cl^- ions are represented by green and violet spheres, respectively. Water molecules are illustrated by the space-filling model (the oxygen atoms are colored dark red) in the SF, the stick model in the NC, and the blue line model in the bulk solution. The KCl concentration was 0.14 M. (B) Free-running perspective of the ion trajectories. The trajectories of repeated ion permeation across the pore are shown along the z-axis as a function of time (t). Between one and three ions occupy the SF simultaneously. An event of an ion entering the SF is termed an SF-in event and is marked by arrowheads.

RESULTS

MD Simulations of the Kv1.2 Potassium Channel. MD simulations of the transmembrane pore domain of a Kv1.2 potassium channel in 0.14 M KCl were performed (Figure 1A). In these simulations, a positive membrane potential of +1000 mV was applied, and the outward K^+ flux was examined. MD simulations at +200 mV were also examined (see SI Figure S1 and Table S1). The root-mean-square of the α-carbon atoms from the X-ray crystal structure was <2.1 Å throughout the simulation. Also, the coordination number of each ion in the SF was very similar to that Egwolf and Roux reported (Figure S2).[26] These facts indicated that the channel remained in its open conformation.

A rough sketch of the motions of the ions from the intracellular solution (IS) to the extracellular solution (ES) features the parts of the permeation pathway or the pore (Figure 1A). K^+ enters the NC from the IS by crossing a constricted sectional area formed by a proline−valine−proline structural motif.[20] K^+ is fully hydrated in the NC[7] and reaches the deepest site of the NC, which is termed the C site. K^+ is mostly dehydrated when it enters the SF.[27] The five binding sites in the SF of the Kv channel are termed S_0 through S_4 and hold multiple K^+ ions simulta-

neously.[27−29] K^+ is immediately hydrated when it exits from S_0 to the ES.

The MD simulation revealed that the NC (including the C site) rarely contains ions (Figure 1B) and generally only up to one ion throughout the simulation time, which was not expected. By contrast, the NC holds approximately 35 water molecules. The infrequent and exclusive occupancy of an ion in the NC was quantified as the time-averaged number of ions, which was 0.24, and the ion concentration in this limited space was 0.38 M. Thus, the K^+ concentration in the NC was greater than that in the bulk solution (0.14 M). The infrequent occupancy on the microscopic time scale and the concentrated K^+ in the time average characterized a feature of the nanocavities.

In the bulk solutions (i.e., the IS and ES), the ions move freely in 3D space, whereas, in the SF, ions move in a single-file manner without passing each other. Moreover, double ion occupancy in the NC is rare with a probability of less than 0.0003, which makes the passing of ions within the NC ignorable. Hereafter, the positions of the ions are expressed on the z-axis along the pore or the channel axis (Figure 1B). Ions repeatedly traverse the pore during the simulation period, and these trajectories along the z−t coordinates are referred to as the "free-running perspective".

In the SF, we frequently observed synchronized stepwise motions of multiple ions (Figure 1B). These stop-and-go motions in the SF have been observed in other potassium channels.[9,10,12−15] During a 2.0-μs simulation, 204 ions were transferred from the IS to the ES (the net ion flux), and the mean interval between ion permeation events (for instance, the interval between the times at which successive ions enter the SF) or the mean permeation time was approximately 9,800 ps. This permeation time corresponds to a single-channel conductance of 16.3 pS (the chord conductance; current amplitude/voltage), being comparable with the experimental data.[17] During the same time period, 215 water molecules were transferred across the pore, yielding a water−ion coupling ratio (water flux/ion flux) of 1.05. At +200 mV, the ratio was 1.0 (Table S1). This value is consistent with the experimentally measured values for other potassium channels (Ca^{2+}-activated, HERG, KcsA, and Kir2.1 channels).[28−31] The agreements between these quantitative data from MD simulations and experimental observations validate our MD simulations.

Event-Oriented Analysis. To examine the permeation process, we developed an event-oriented analysis method, in which the permeation processes were traced anterogradely and retrogradely in time from an arbitrary event (Figure 2). First, we defined an event along the MD-simulated ion trajectories (free-running perspective). The event of K^+ entering the SF (the S_4 site) from the NC (the C site) causes a distinct transition and was repeatedly observed in the free-running perspective. Thus, this event (SF-in event) is an appropriate marker in a trajectory (arrowheads in Figure 1B). Stochastic ion trajectory paths are aligned by adjusting the time of the SF-in event (event-synchronized sample paths; Figure 2A, B), by which the time courses of ions approaching to the event and subsequent processes from the event can be collectively analyzed (convergence and divergence to and from the event).

First, we followed the anterograde process from the SF-in, which reproduced the previous studies. In the event-oriented analysis, each ion that entered the SF was classified as I_0. Prior to the entry of I_0, two ions were already present in the SF (Figures 1B and 2A). The ion that entered immediately before I_0 was termed I_1 (blue), and the ion that entered immediately before I_1 was termed I_2 (green). During the time range of ±20 ps from the
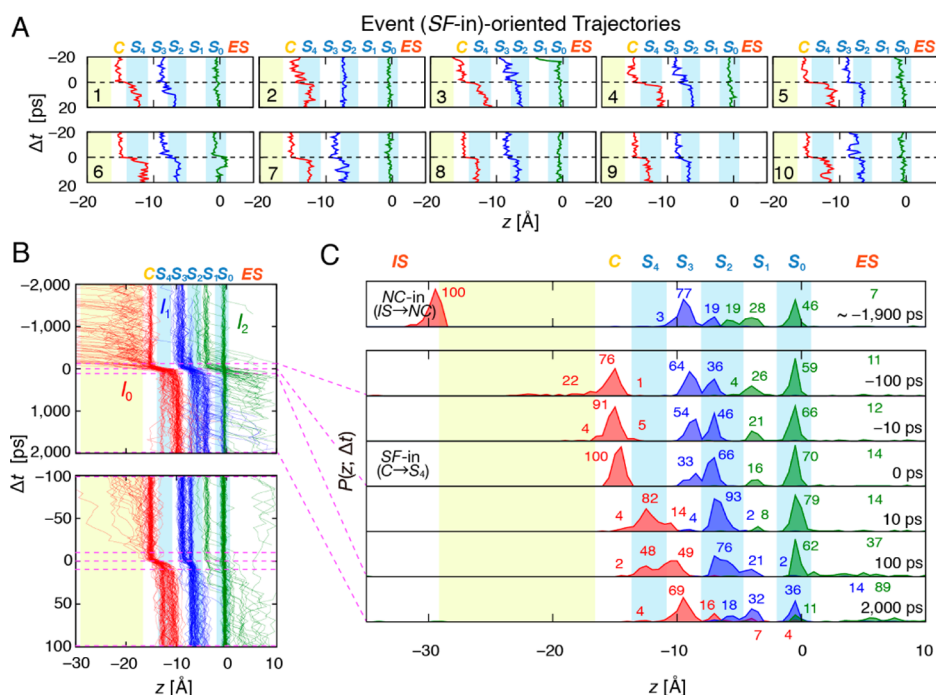
Figure 2. Event-oriented trajectories and distributions of multiple ions in the pore. (A) Event-oriented trajectories. The moment of the *SF*-in event was set to $\Delta t = 0$ (the transition from the *C* site to the S_4 site occurs during $0 < \Delta t < 1$ ps). Representative trajectories of the three ions shown in Figure 1B are shown 20 ps before and after the *SF*-in moment (panels 1−10). The *SF*-in ion, I_0, is plotted in red, the ion that enters before I_0 (I_1) is in blue, and the ion that enters before I_1 (I_2) is in green. (B) Superimposed event-oriented trajectories. The top panel shows the trajectories 2,000 ps before and after the *SF*-in moment, and the bottom is an enlarged view (±100 ps) At negative Δt, I_0 moved across the *NC* and reached the deepest site of the *NC* (the *C* site), whereas I_1 remained primarily in S_3 and I_2 occupied either S_1 or S_0. At positive Δt, I_0 remained in S_4, I_1 moved to S_2, and some I_2 left the pore. (C) Event-oriented distributions. Spatial distributions of I_0, I_1, and I_2 along the *z*-axis at either positive or negative Δt. The bin size was 1 Å⁻¹. The numbers next to the distribution peaks denote the probabilities in percentages of each ion being at a defined site. The distributions before (−100 ps) and after (2,000 ps) the *SF*-in moment are shown. The moments corresponding to the trajectories in (B) are marked by dashed magenta lines. Further backward tracing leads to the moment when I_0 entered the *NC* at $\Delta t \sim -1,900$ ps (*NC*-in; the top panel).

SF-in moment, the trajectories for the three ions were collected (event-oriented sampling) and aligned around the *SF*-in moment ($\Delta t = 0$; Figure 2A). Correlated motions of I_0, I_1, and I_2 were clearly observed around the *SF*-in event.

All event-oriented trajectories were superimposed for 2,000 ps before and after the *SF*-in moment to reveal the ensemble behavior of the I_0, I_1, and I_2 displacement around the *SF*-in moment (Figure 2B, top panel). The trajectories with the expanded time scale (100 ps before and after the *SF*-in event; Figure 2B, bottom) clearly show the sequence of events. The S_3-occupied I_1 (I_1^{S3}, where the superscript represents the position of the ion) shifted its position outward to S_2 roughly coincidently with the shift of I_0 at $\Delta t = 0$.

Event-Oriented Distribution. Ion shifts were quantified by evaluating the positional distributions of the I_0, I_1, and I_2 ions along the *z*-axis at different Δt, $P(z; \Delta t)$ (Figure 2C).[32] Accordingly, the evolution of distributions at a time from the *SF*-in event can be followed. At $\Delta t = 0$, I_0 (red) was positioned at the *C* site by definition, whereas I_1 (blue) was located at either S_3 or S_2, and I_2 (green) predominantly occupied S_0 rather than S_1. Immediately after the *SF*-in moment, the *SF* contained three ions simultaneously. This unfavorable state was relaxed via outward shifts of the three ions, leading to the expulsion of the outermost ion toward the *ES* (outward run). This sequence of events happening around the *SF* space, from the *SF*-in moment to the departure of I_2, has been previously referred to as the "knock-on" process.[8,9,12−15]

Next, ion movements *before* the *SF*-in moment were examined. The ion distributions were traced backward from $\Delta t = 0$

(retrograde tracing). The probability of I_1^{S3}, $P(I_1^{S3})$, was higher at $\Delta t = -10$ ps than at $\Delta t = 0$ and higher still at $\Delta t = -100$ ps, indicating surprisingly that I_1 and I_2 had already initiated their outward shifts before the *SF*-in moment. This mechanism has not been expected in the knock-on mechanism. Retrograde tracing continued until the *NC*-in moment, when I_0 entered *NC* (*NC*-in event). The ion distribution is shown in the top panel of Figure 2C (see also Figure S3). When measured from the *SF*-in moment, the *NC*-in event occurred at $\Delta t = 1,900$ ps on average.

At the *NC*-in moment, the probability of I_2 in the *SF* was 93%, indicating that 7% of the channel did not contain I_2 (Figure 2C). I_2 exited the *SF* before I_0 entered the *NC*, and the *SF* contained only one ion. A sample trajectory is presented in panel 9 of Figure 2A. A one-ion permeation mode is predicted in MacKinnon's model[27] and has been proven experimentally by measurements of streaming potential.[28−31]

The Run-after Mechanism. The gradual outward trends of the ion distributions (Figure 2C) indicate that the ion motions are roughly concerted on the nanosecond time scale. In contrast to this coarse view, each ion moves more or less independently on the picosecond time scale. The flux of each ion was calculated from the ion distributions. At negative Δt, I_0 is located at *NC* (mainly *C*), whereas it is distributed at S_4 or S_3 at positive Δt. Thus, the probability of I_0 remaining in the upstream position (P^{up}) can be defined by setting a boundary between the *C* and S_4 sites. The P^{up} of I_0 (P_{I0}^{up}; red) was 100% before the *SF*-in moment, whereas, for $\Delta t > 0$, a stepwise decrease followed by gradual decay was observed (Figure 3A, and Figure S4 with an expanded time scale). Similarly, P_{I1}^{up} (blue) and P_{I2}^{up} (green)

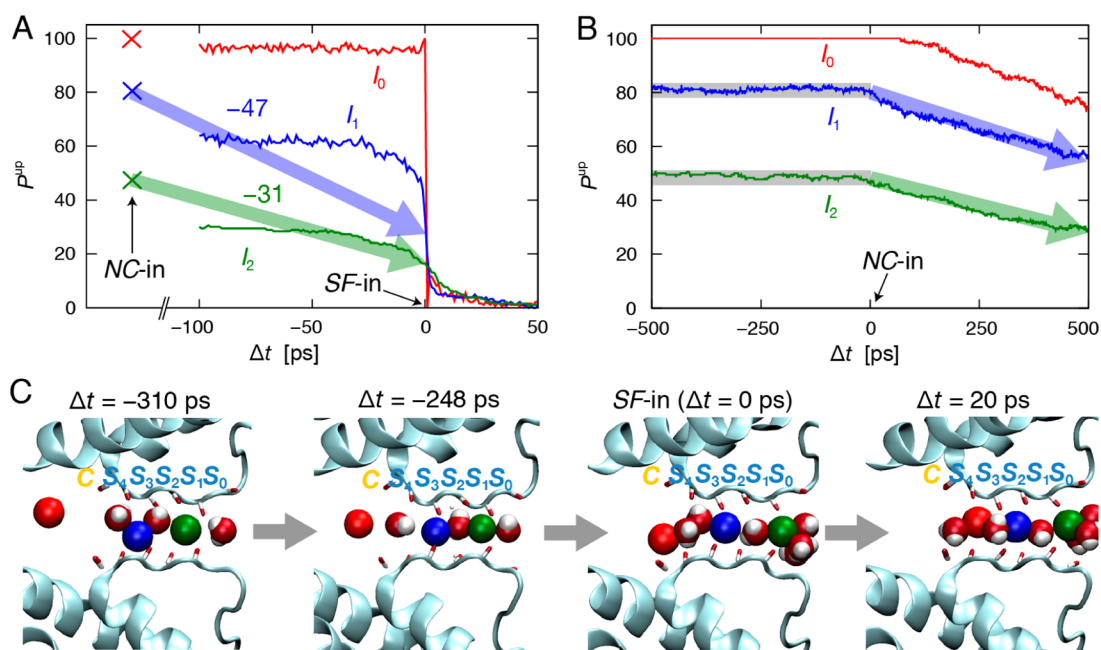**Figure 3.** Flux of each ion in the pore. (A) The probability of ions occupying upstream positions (P^{up}) as a function of Δt from the SF-in moment. P_{I0}^{up} is $P(I_0^{IS}) + P(I_0^{NC})$ (red), P_{I1}^{up} is $P(I_1^{S4}) + P(I_1^{S3})$ (blue), and P_{I2}^{up} is $P(I_2^{S2}) + P(I_2^{S1})$ (green). The time derivative of P^{up} determines the flux of the relevant ion. (B) Time-dependence of P^{up} around the NC-in event. P_{I0}^{up}, P_{I1}^{up}, and P_{I2}^{up} are as defined above. The P_{I1}^{up} and P_{I2}^{up} values remain constant before the NC-in moment but begin to decay after the NC-in moment. (C) Snapshots of ions and water in the pore. At negative Δt, I_1 shifted from S_3 to S_2 and left a vacant space at S_3, which was then filled by a water molecule. The carbonyl oxygens of the SF backbone and threonine OH are shown in dark red.

were defined by setting a boundary between S_3 and S_2 and between S_1 and S_0, respectively. Upon the SF-in moment, P_{I1}^{up} also displayed a stepwise decrease to half of its previous value (Figures 3A and S4). By contrast, P_{I2}^{up} exhibited a gradual rather than a stepwise decrease.

At the time of NC-in, P_{I1}^{up} was 80%, which was followed by a gradual decrease to a plateau for several tens of picoseconds before the SF-in moment. The outward shifts subsequently accelerated, notably within the time range of 20 ps immediately before the SF-in moment. Similar behavior was observed for I_2. This acceleration immediately before the SF-in moment suggests that I_1 and I_2 prepared for the motion, as if they had "predicted" the moment of the I_0 shift. A more reasonable interpretation of this I_1 and I_2 behavior is that the preceding I_1 and I_2 motion allowed the SF-in movement of I_0.

Snapshots at times near the SF-in moment illustrate the shifting motions of the SF ions, with a water molecule intercalated between ions (Figures 3C and S5, Movies S1−3). At negative Δt, I_1 occupied S_3, and a water molecule occupied S_4. When I_1^{S3} moved to S_2 before the SF-in moment, the water remained at S_4; thus, a vacant space was formed behind I_1 at S_3. This vacant space was subsequently filled by the water molecule in S_4 upon SF-in. These events on the picosecond time scale suggest a mechanism in which the downstream ions move earlier and are followed by movement of the upstream ion (the "run-after" mechanism). Unlike the "knock-on" mechanism, this is reminiscent of the theoretical model called the vacancy model.[33] After the SF-in moment, the time courses of changes in P^{up} were comparable for all three ions (Figure 3A), suggesting a concerted shift of the ions at this time scale.

The event-oriented analysis is a powerful tool to examine a chronological order of events. The run-after mechanism is further supported by defining the event of I_1 motion from S_3 to S_2 for event-oriented analysis (Figure S6), and similar preceding shifts of I_1 and I_2 were observed. Moreover, the run-after

mechanism was also observed at +200 mV; MD simulation was performed at +200 mV, and the results indicated that the movements of I_1 and I_2 preceded those of I_0 (Figure S1). The gradual outward shifts of I_1 and I_2 even at +200 mV indicate that the strong membrane electric field of +1000 mV was not the major force driving the preceding shifts of the ions in the SF.

When do the ions in the SF initiate their outward shift? This simple question has not even been raised in the earlier studies. In the previous section, the gradual outward shift of ions in the SF was traced back to the NC-in moment. The changes in P^{up} before and after the NC-in moment were plotted (Figure 3B). Outward shifts of I_1 and I_2 were observed exclusively after the NC-in moment (Figures 3B and S3). This finding indicates that the NC-in of I_0 is a critical event that initiates the outward motion of I_1 and I_2 in the SF via a coherent interaction between the ions in the NC and SF, or in the entire pore.

Coherent Interaction across the Entire Pore. To fully understand the coherent actions of the ions, we focused on determining how the ions in the SF sensed when an ion had entered the NC and initiated their subsequent outward runs. Thus, we calculated the potential energy profile of individual I_1 and I_2 ions during the ion-unoccupied period (solid line) and ion-occupied period (broken line) of the NC (Figure 4A; Figure S7 for the period from the NC-in to the moment when I_0 reaches the C site). When I_0 was absent from the NC, I_1 stably remained at either S_3 or S_2. By contrast, when I_0 was present in the NC, the potential profile at the S_3 site was increased by 9 kcal/mol, with a concomitant attenuation of the barrier height toward the S_2 site, prompting the transfer of I_1 to the S_2 site. Similarly, the energy level of I_2 at S_2 was increased by 3 kcal/mol when I_0 was present in the NC. These results suggest that the presence of I_0 in the NC can effectively repel I_1 and I_2 to outward locations in the SF.

Here we address how the ions in the SF experience a repulsive force from an ion in the NC even under the presence of water. The NC is a nanocavity bearing a total of approximately 35 water
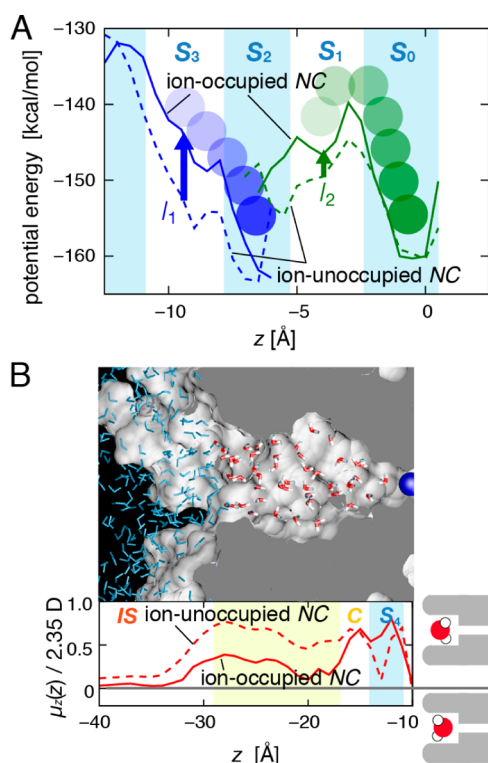
Figure 4. Coherent interactions of ions. (A) Potential energy profiles for I_1 and I_2 during the ion-unoccupied NC (broken line) and ion-occupied NC (solid line) periods; the derivative of the potential energy with respect to z is the force acting on the ion. When I_0 was in the NC, the potential of I_1 at S_3 increased by 9 kcal/mol, leading to an outward displacement of I_1. Similarly, I_2 in S_1 was destabilized. (B) NC water and its dipole moment. A snapshot of water in the ion-unoccupied NC is shown. The mean z-component of the dipole moment of the water along the z-axis ($\mu_z(z)$) is shown after normalization using the TIP3P water dipole (2.35 D). The positive sign indicates that the water dipoles point toward the SF (right upper cartoon). The $\mu_z(z)$ is indicated by a broken line during the ion-unoccupied NC period and by a solid line during the ion-occupied NC period. Even in the presence of an ion, the water dipoles point toward the SF and cannot completely shield the repulsive force between I_0 and I_1.

molecules (Figure 4B, upper panel); hence, the configurations of the water molecules in it likely differ from those in the bulk solution.[7,10] The dipole orientation of the water molecules in the NC was examined. The broken line along the z-axis in Figure 4B (Figure S8 for the SPC/E water) represents the z-component of the dipole moment of water in the absence of an ion in the NC. The positive values of the profile indicate that the water dipoles point toward the SF (Figure 4B, right panel, upper cartoon). This water orientation is weakened but not abolished when an ion occupies the NC (solid line). During I_0 travel across the NC, water molecules in the NC rearranged to permit hydration, and the dipole moment of water should therefore be similar to that in the bulk solution. However, the dipole moment remained positive, probably because of the continued interaction between the water and the channel (see below). Consequently, the water did not completely shield the electrostatic repulsion between I_0 in the NC and the ions in the SF (Tables S2 and S3), and the ions in the SF were able to initiate their escape motion when I_0 entered the NC.

The origin of the oriented water in the NC was examined in the simulation. When the dipoles of the pore helix are annihilated, the water orientation is substantially weakened (Figure S8 orange

line). On the other hand, the water orientation was not vanished in the absence of voltage (Figure S8 cyan line). These results indicate that the water orientation is mostly due to interactions with the macrodipole of the pore helix.[34] The hydrophobic surface of the NC readily allows this orientation.

We revealed that the NC, filled with the structured water, is more involved in the ion permeation rather than simply bearing an ion.

Cyclic Reaction Phase Diagram. In the previous section, the NC-in event has been described using retrograde tracing from the SF-in moment (Figure 2C), but the NC-in event (for the next incoming ion) can also be reached using anterograde tracing from the SF-in moment. Accordingly, the permeation process is completed as a cycle, and we constructed a cyclic reaction phase diagram for the permeation (Figure 5). The NC-in and SF-in
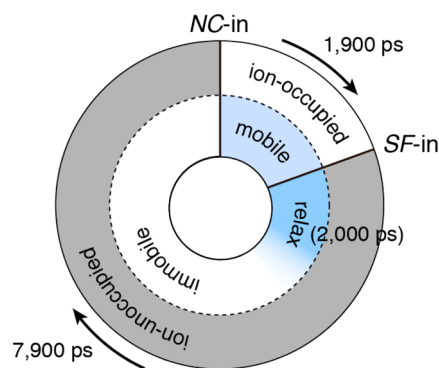

Figure 5. Cyclic reaction phase diagram for permeation through the Kv channel. The outer and inner rings represent the status of the ions in the NC and the SF ions, respectively. Outward permeation processes proceed clockwise. The NC-in and SF-in are epoch-making events whose moments are precisely defined and divide the cycle into two phases. After an ion enters the NC (ion-occupied NC), the ions in the SF begin to shift outward (mobile phase). Meanwhile, this ion entrance increases the number of ions in the SF to three. These three ions in the metastable state are gradually redistributed outward with a relaxation time (relaxation), thus expelling the downstream ion. After the relaxation, the ions in the SF maintain their position (immobile phase). After the SF-in moment, the NC is empty until the next NC-in moment (ion-unoccupied NC). The mean periods in the ion-occupied, ion-unoccupied, and relaxation phases for a K$^+$ concentration of 0.14 M are shown. The dwell times are represented by arc lengths. Thus, the events are transition states and the phases are intermediate states.

events are epochs of permeation. Alternate transitions between these two events generate the net ion flux. Thus, these distinct events delimit two periods of time in the cyclic phase diagram.

The permeation is expressed using two concentric rings: the outer ring for ion-occupancy states in the NC and the inner ring for the status of ions in the SF. An ion in the IS approaches and enters the NC at the NC-in moment by crossing the barrier at the NC entrance, and permeation then proceeds in a clockwise manner around the rings. The event-oriented trajectories allow measurements of the time periods between the transitions. Until the SF-in moment, the NC was ion-occupied for 1,900 ps (the ion-occupied NC phase), while the ions in the SF moved outward due to the electric repulsive effect across the NC (the ion-mobile phase). After the SF-in moment, the NC was empty (the ion-unoccupied NC phase). When an additional ion entered the SF, three ions occupied the SF; this condition is unfavorable (metastable), causing the ions to shift outward until the expulsion of the outermost ion. Meanwhile, a new ion entered

the NC (the NC-in event) when the cyclic reaction was complete, and the mean cycle time was 9,800 ps (see the section MD Simulations of the Kv1.2 Potassium Channel).

Given the mean time of 1,900 ps from the NC-in moment to the SF-in moment ($t_{NC\text{-}SF}$), the mean time from the SF-in moment to the NC-in moment ($t_{SF\text{-}NC}$) should be 7,900 ps. During this long period of time, the NC remained unoccupied (i.e., the ion-unoccupied NC period), whereas the ions remaining in the SF gradually immobilized and reached a steady-state distribution (the relaxation phase). When is relaxation terminated? A closer examination of the ion distributions at Δt = 2,000 ps after the SF-in moment and at the NC-in moment (Figures 2C and S9) revealed that these ion distributions are superimposable; this superposition corresponds to one shift outward of the relevant ions (the red ion distribution becomes the blue, and the blue becomes the green). Consequently, the relaxation time was only 2,000 ps, and the ion distributions in the SF were subsequently held until the next NC-in moment for the long period of 5,900 ps (i.e., the ion-immobile phase). More than half of the cycle time is thus spent in this ion-immobile phase.

In the phase diagram, the "knock-on" starts from the SF-in event and ends with the exit of I_2, and the average time from the SF-in moment to the exit of I_2 was 1,000 ps (the remaining ions in the SF were relaxed for another 1,000 ps). Thus, the "knock-on" mechanism is indeed a part of the relaxation process, using only one tenth of the mean cycle time.

The diagram indicates the phases and their transitions with their dwell times[35] and readily characterizes the entire permeation process. The microscopic ion trajectories during permeation are integrated into the simplified phases, and the progression of each phase around the cycle is closely interrelated for the NC- and SF-rings. The cyclic reaction phase diagram describes all aspects of permeation at the mesoscopic level (detailed changes in the ion occupancy states in the ion-mobile phase are shown in Figure S10; the positions of I_0, I_1, and I_2 at different times of the cycle are plotted in Figure S11).

Concentration-Dependent Cyclic Phase Diagrams. All simulations hitherto in this study were performed at a physiological K$^+$ concentration (0.14 M). To determine the rate-limiting steps of the permeation at different K$^+$ concentrations, cyclic reaction phase diagrams were constructed. MD simulations were performed at three additional K$^+$ concentrations (0.05, 0.54, and 0.99 M), and event-oriented analysis and subsequent procedures were conducted (Figure S12–14 for the ion distributions at different Δt relative to the SF-in and NC-in moments, Table S4). Even at 0.99 M, the probability of double ion occupancy of the NC, which corresponds to the concentration of more than 3 M, was quite low (less than 0.05). The cyclic phase diagram was simplified to a one-ring representation (Figure 6A), that includes the NC-in and SF-in events. The transitions between these events are indicated using two arrows: a gray arrow for the NC-in → SF-in transition and a dark arrow for the SF-in → NC-in transition. The arc length of each of these arrows corresponds to the time spent in each transition ($t_{NC\text{-}SF}$ and $t_{SF\text{-}NC}$; or the ion-occupied and -unoccupied NC periods), such that the total circumference represents the cycle completion time (t_{perm}). The inverse of t_{perm} represents the K$^+$ flux (J_K). Similarly, the inverses of $t_{NC\text{-}SF}$ and $t_{SF\text{-}NC}$ represent the transition rates between the NC-in and SF-in events, which are denoted $k_{NC\text{-}SF}$ and $k_{SF\text{-}NC}$, respectively.

As the K$^+$ concentration increased from 0.05 to 0.99 M, the cycle size decreased markedly. The plot of the concentration-dependent J_K values (Figure 6B) reveals a Michaelis–Menten-
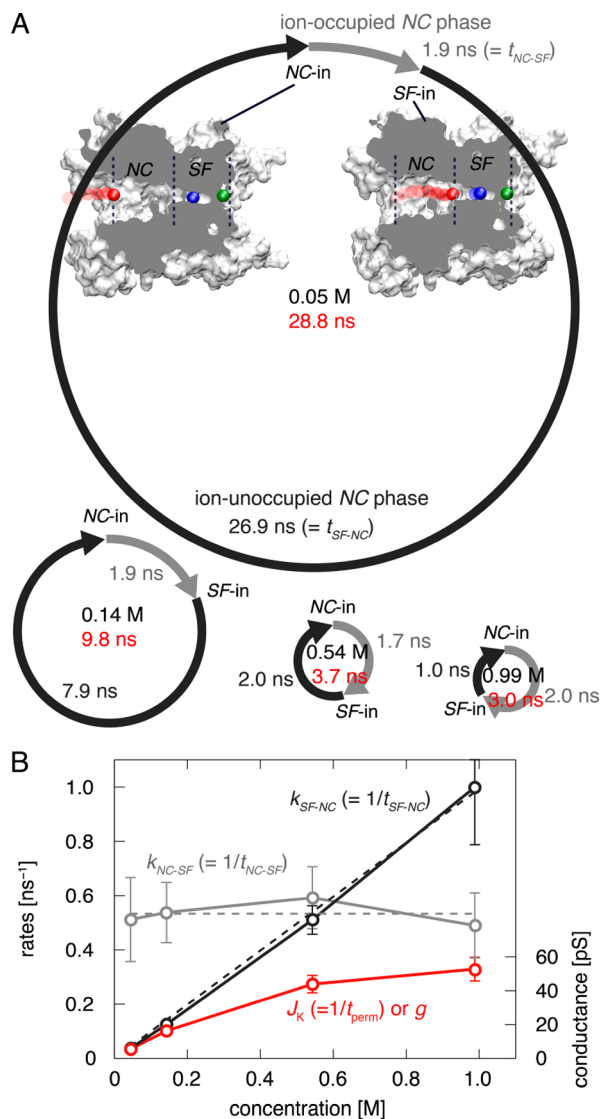

Figure 6. K$^+$ concentration dependence of the cyclic reaction phase diagram and permeation rates. (A) Simplified cyclic reaction phase diagrams at different K$^+$ concentrations. The MD simulations were performed at K$^+$ concentrations of 0.05, 0.14, 0.54, and 0.99 M, and the simplified cyclic reaction phase diagrams, a single ring involving the ion-occupied (NC-in−SF-in) period ($t_{NC\text{-}SF}$; gray arrow) and the ion-unoccupied (SF-in−NC-in) period ($t_{SF\text{-}NC}$; black arrow), are shown. As the K$^+$ concentration increased, the circumference representing the permeation cycle time (t_{perm}: red number at the center of the cycles) decreased, whereas the ion-occupied period remained nearly unchanged; thus, the ion-unoccupied period decreased dramatically. (B) Concentration dependence of the rates. The rates are expressed as the inverses of the periods. The ion flux (J_K) was defined as the inverse of t_{perm} and exhibited saturating behavior, thereby reproducing the reported experimental data. The inverse of $t_{SF\text{-}NC}$ is proportional to the concentration (the dashed black line), the slope of which is the rate of filling the NC ($k_{SF\text{-}NC} = k*_{SF\text{-}NC}C$). The inverse of $t_{NC\text{-}SF}$ is constant throughout the concentration range (the dashed gray line). The standard deviation of each data point estimated by block averaging is shown when larger than the size of the data points.

type saturating curve and reproduces experimental data previously reported for the Kv channel.[17] $k_{SF\text{-}NC}$ increased linearly as the concentration increased, whereas $k_{NC\text{-}SF}$ was nearly constant throughout the concentration range (Figure 6B). These results indicate that, at low K$^+$ concentrations, the filling of the

NC limits J_K. By contrast, at high K^+ concentrations, the rate of ion transfer across the NC to the SF determines J_K.[36]

DISCUSSION

The cyclic phase diagram provides a comprehensive picture of ion permeation through the Kv1.2 channel that completely revises the previous understanding of the ion permeation mechanism through potassium channels, including the knock-on mechanism. We conclude that permeation throughout the entire pore proceeds via a sequence of microscopic events involving remote repulsion, run-after, relaxation, and queueing, resulting in mesoscopic mobile and immobile phases. To integrate these micro- and mesoscopic events, the digitalized occupancy of K^+ in the NC serves a role for catalytic action of permeation. First of all, the K^+ concentration in the IS is digitalized in the NC. In the "zero" state (or the ion-empty in the NC), the ions in the SF were held (queueing). In the "one" state (or the ion-occupied in the NC), the queueing is released through the structured water in the NC. Thus, the frequency of occurrence of the "one" state governs the permeation rate. The integrated cyclic phase diagram provides an overall picture of permeation, accounting for the experimentally obtained concentration-dependent single-channel current amplitude.

In this study, we established a systematic method that begins with event-oriented analysis, followed by construction of the cyclic phase diagram via an event-oriented distribution. This process straightforwardly extracts a chronological order of events and rates[37−39] from ion trajectories. In addition to capturing events and event transitions with variable time scales, the advantages of the method include retrograde tracing that revealed the unprecedented remote repel feature of the permeation process. This systematic method could be widely applied to the analysis of stochastic trajectories, including data from single-molecule measurements.[5,40,41]

We have previously performed electrophysiological experiments to evaluate the water−ion flux ratio through potassium channels[28,29,31] and have examined the underlying permeation processes with a theoretical method called cycle flux algebra.[42,43] The experimental data on single-channel currents and the water−ion flux ratios were integrated in the analysis, and the permeation process was decomposed into cyclic processes in a discrete-state permeation diagram.[29] In the present study, the microscopic trajectories were integrated into a cyclic reaction formula. Overall, our previous attempts using a top-down strategy and the current bottom-up strategy converge at the mesoscopic level.

In this study, we highlighted the unexpected roles of the nanocavity. The infrequent ion occupancy in the NC, which is unexpected for most physiologists, has not been clearly described in previous reports. In the cyclic phase diagram, the involvement of the ion occupancy state in the NC allowed us to explain the saturation behavior of the conductance−concentration relationship. This behavior displayed Michaelis−Menten-type enzyme kinetics.[44] The NC remains empty for a long queueing period, and once occupied by an ion, consecutive processes begin. The ion-bearing NC is a reaction intermediate for the subsequent catalytic action.

The NC is shared by K^+ channel structures, and the functional role of the NC can be generalizable to some extent. The NC of the Kv1.2 channel is relatively small sized with neutral surface charge, while that of MthK is large and that of BK is negatively charged.[22,45−47] These geometrical and electrostatic varieties render the role of the NC variable in the ion permeation, and detailed studies for the NC are necessary in the future. In addition to channels, nanocavities are frequently found in proteins, especially transporter proteins.[48] The roles of the NC in ion transport processes remain an open question to be examined.

MATERIALS AND METHODS

System Preparation. The system at 0.14 M was composed of one Kv1.2 channel, 119 dioleoylphosphatidylcholine (DOPC) lipids, 30 K^+, 22 Cl^-, and 10520 water molecules (see Table S4 for other concentrations). First, the DOPC bilayer was equilibrated with the surrounding KCl solution for 10 ns. The MD simulation was performed using the NPT ensemble (1 bar, 310 K) with Berendsen's barostat.[49] The area per lipid after equilibrium was confirmed to be the same as previously reported.[50] The DOPC and the solution overlapping with the pore domain (residues 312−421) of the Kv1.2 channel (PDB code: 2A79)[51] were removed to incorporate the channel. An equilibrium simulation was performed for 10 ns using the NPT ensemble (1 bar, 310 K) in which α-carbons were under the influence of a weak harmonic constraint (0.25 kcal/mol/Å^2). The simulation of equilibration using the NVT ensemble (310 K) with Berendsen's thermostat[49] continued for 10 ns after the constraint on the Kv1.2 channel was removed.

Molecular Dynamics Simulations. The following empirical potentials were used: the TIP3P model for water, the ff94 force field for the channel, the Dang model for K^+ ions, and the Siu model for lipids.[50,52−54] The SPC/E model for water and the ff99SB force field for the Kv1.2 channel were also examined (see Table S1).[55,56] A total of 50 independent initial coordinates were generated and were evolved over time according to Newton's equations of motion.

MD simulations were performed at constant volume and temperature (310 K) using Berendsen's thermostat.[49] A periodic boundary condition of 78.0 × 81.2 × 85.0 Å^3 was imposed. Long-range interactions were calculated using the particle-mesh Ewald method[57] with an 8-Å real-space cutoff. The bonds, including those for H atoms, were constrained using the SHAKE algorithm,[58] enabling a time step of 2 fs.

The *sander* module in the AMBER11 package was modified to apply the electric field and was used to observe passive ion transport.[59] The electric field was applied to mimic a voltage-clamp experiment:[60] a voltage of 800 mV was applied to the SF (14 Å) and that of 200 mV was applied to $NC + IS$ (19 Å: 15 Å in NC and 4 Å in IS) (Figure 1A).[61] MD simulations were performed for 100 ns for ten configurations and for 25 ns for 40 configurations at 0.14 M.

Definitions of the SF-in and NC-in Times. The SF-in moment was defined as the moment when an ion in the NC crossed a border toward the SF and reached S_4 (arrowheads in Figure 1B). First, the border between NC and SF was defined as the position of the side chain oxygen in Thr374: $z = -14.1$ Å, where z is the channel axis (Figure 1). Typically, SF-in moments were clearly observed (indicated as arrows in Figure S15A). Occasionally, recrossings were observed,[38] such as when I_0 transiently entered the S_4 site and immediately returned to the NC; these recrossings were not used to determine the SF-in time (Figure S15B). Transient visits of less than 20 ps were not counted as SF-in events. Instead, only transitions that led to a steady dwelling in S_4 were defined as SF-in events. Changing the window of the transient dwell time at the S_4 site altered the SF-in moment but had a negligible effect on the period of each phase.

For the NC-in moment, the border between the IS and the NC was set as the most constricted position along the cavity, the site of the proline-valine-proline structural motif at $z = -29.0$ Å. Recrossings were occasionally observed but were not used to determine the NC-in time.

The time from the NC-in moment, t_{NC}, to the SF-in moment, t_{SF}, was calculated as $t_{SF} - t_{NC}$ for each permeation event. This time is equal to $t_{NC\text{-}SF}$. The mean time of ion permeation was also estimated by subtracting the t_{NC} of a permeation event from the t_{NC} of the next permeation event.

Probability of an Ion at Each Site. The borders between S_4 and S_3, S_3 and S_2, S_2 and S_1, S_1 and S_0, and S_0 and the ES were set as the positions of the carbonyl oxygens of Thr374, Val375, Gly376, Tyr377, and Gly378, respectively. The respective z-coordinates were −10.9 Å, − 7.8

Å, − 5.1 Å, − 2.1 Å, and 0.9 Å. The C site, the deepest site in NC, was set as the region 2.5 Å upstream of the border between the NC and the SF.

The probability of an ion existing at each site ($P(I)$) was evaluated as a percentage using the integral of $P(z; \Delta t)$ at the relevant site. For example, the probability of I_1 at the S_3 site, $P(I_1^{S3})$, was calculated using the following equation,

$$P(I_1^{S3}) = 100 \times \int_{-10.9}^{-7.8} P_{I1}(z; \Delta t)dz$$

where $P_{I1}(z; \Delta t)$ is $P(z; \Delta t)$ of I_1.

Upstream Probability, P_{up}. Due to the definition of the SF-in moment, I_0 jumps into S_4 from the C site at $\Delta t = 0$. Accordingly, the upstream probability, P^{up}, for I_0 (P_{I0}^{up}) is $P(I_0^{IS}) + P(I_0^{NC})$. During the time surrounding the SF-in moment, I_1 moves from S_4 or S_3 to S_2, S_1, or S_0; $P(I_1^{S4})$ and $P(I_1^{S3})$ decrease at $\Delta t = 0$, while $P(I_1^{S2})$, $P(I_1^{S1})$, and $P(I_1^{S0})$ increase at $\Delta t = 0$. Accordingly, P_{I1}^{up} is defined as the sum of the probability of the ion distributions in the upstream positions (S_4 or S_3), giving $P_{I0}^{up} = P(I_1^{S4}) + P(I_1^{S3})$. Similarly, $P_{I2}^{up} = P(I_2^{S2}) + P(I_2^{S1})$.

Calculation of the Potential Energy Profile. The potential energy profile of an ion along the z axis, $\langle E(z) \rangle$, was calculated by using the following equation:

$$\langle E(z) \rangle = \int_0^{box_Z} \int_0^{2\pi} \int_0^{\infty} \delta(z - z')E e^{-H/k_B T} r dr d\theta dz'$$

where box_Z, H, k_B, T, r, and θ are the cell size of the system along z axis, the Hamiltonian of the system, the Boltzmann constant, the temperature, the radial coordinate that is perpendicular to the z axis, and the azimuthal angle, respectively. The brackets indicate an ensemble average. E is the interaction between an ion at a certain z and the system. The derivative of E with respect to z gives the force acting on the ion.

Snapshots and Movies. All snapshots and movies were produced using the Visual Molecular Dynamics package.[62]

ASSOCIATED CONTENT

Ⓢ Supporting Information

The Supporting Information is available free of charge on the ACS Publications website at DOI: 10.1021/jacs.6b05270.

> Time course of the ion distribution and the P^{up} values; coordination numbers for a K$^+$ ion in the pore; NC-in oriented distribution; close-up view of P^{up}; event-oriented trajectory of I_0, I_1, and I_2; ion distribution before and after the transition of I_1 from S_3 to S_2; potential energy profile as a function of z; z component of the mean water dipole moment; relaxation process from the SF-in moment; ion occupancy states and the transitions among them in the ion-mobile phase; progression of I_0 and I_1 along the 2-dimensional free energy surface during one permeation cycle; event-oriented distributions at 0.05 M K$^+$, at 0.54 M K$^+$, and at 0.99 M K$^+$; SF-in oriented trajectories; MD simulation conditions; energy change of I_1 at S_3; energy change of I_2 at S_1; and ion permeation (PDF)
>
> Movie of the ion permeation through the SF (AVI)
>
> Movie of the ion permeation through the SF with 1 ps sampling time (AVI)
>
> Movie of the ion permeation through the SF with 0.1 ps sampling time (AVI)

AUTHOR INFORMATION

Corresponding Author

*oiki-fki@umin.ac.jp

Notes

The authors declare no competing financial interest.

ACKNOWLEDGMENTS

REFERENCES

(1) Hille, B. *Ion Channels of Excitable Membranes*, 3rd ed.: Sinauer: Sunderland, MA, 2001.
(2) González, B.; Baez-Nieto, D.; Valencia, I.; Oyarzún, I.; Rojas, P.; Naranjo, D.; Latorre, R. *Compr. Physiol.* **2012**, *2*, 2087−2149.
(3) Oiki, S. *J. Physiol.* **2015**, *593*, 2553−2573.
(4) Yifrach, O.; MacKinnon, R. *Cell* **2002**, *111*, 231−239.
(5) Shimizu, H.; Iwamoto, M.; Konno, T.; Nihei, A.; Sasaki, Y. C.; Oiki, S. *Cell* **2008**, *132*, 67−78.
(6) Doyle, D. A.; Morais-Cabral, J.; Pfuetzner, R. A.; Kuo, A.; Gulbis, J. M.; Cohen, S. L.; Chait, B. T.; MacKinnon, R. *Science* **1998**, *280*, 69−77.
(7) Guidoni, L.; Torre, V.; Carloni, P. *FEBS Lett.* **2000**, *477*, 37−42.
(8) Bernèche, S.; Roux, B. *Nature* **2001**, *414*, 73−77.
(9) Khalili-Araghi, F.; Tajkhorshid, E.; Schulten, K. *Biophys. J.* **2006**, *91*, L72−L74.
(10) Domene, C.; Vemparala, S.; Furini, S.; Sharp, K.; Klein, M. L. *J. Am. Chem. Soc.* **2008**, *130*, 3389−3398.
(11) Furini, S.; Domene, C. *Proc. Natl. Acad. Sci. U. S. A.* **2009**, *106*, 16074−16077.
(12) Jensen, M. Ø.; Borhani, D. W.; Lindorff-Larsen, K.; Maragakis, P.; Jogini, V.; Eastwood, M. P.; Dror, R. O.; Shaw, D. E. *Proc. Natl. Acad. Sci. U. S. A.* **2010**, *107*, 5833−5838.
(13) Kasahara, K.; Shirota, M.; Kinoshita, K. *PLoS One* **2013**, *8*, e56342.
(14) Jensen, M. Ø.; Jogini, V.; Eastwood, M. P.; Shaw, D. E. *J. Gen. Physiol.* **2013**, *141*, 619−632.
(15) Köpfer, D. A.; Song, C.; Gruene, T.; Sheldrick, G. M.; Zachariae, U.; de Groot, B. L. *Science* **2014**, *346*, 352−355.
(16) Hodgkin, A. L.; Keynes, R. D. *J. Physiol.* **1955**, *128*, 61−88.
(17) Heginbotham, L.; MacKinnon, R. *Biophys. J.* **1993**, *65*, 2089−2096.
(18) LeMasurier, M.; Heginbotham, L.; Miller, C. *J. Gen. Physiol.* **2001**, *118*, 303−314.
(19) MacKinnon, R.; Latorre, R.; Miller, C. *Biochemistry* **1989**, *28*, 8092−8099.
(20) Webster, S. M.; del Camino, D.; Dekker, J. P.; Yellen, G. *Nature* **2004**, *428*, 864−868.
(21) Geng, Y.; Niu, X.; Magleby, K. L. *J. Gen. Physiol.* **2011**, *137*, 533−548.
(22) Díaz-Franulic, I.; Sepúlveda, R. V.; Navarro-Quezada, N.; González-Nilo, F.; Naranjo, D. *J. Gen. Physiol.* **2015**, *146*, 133−146.
(23) Shim, J. W.; Gu, L.-Q. *J. Phys. Chem. B* **2008**, *112*, 8354−8360.
(24) Rasaiah, J. C.; Garde, S.; Hummer, G. *Annu. Rev. Phys. Chem.* **2008**, *59*, 713−740.
(25) Stank, A.; Kokh, D. B.; Fuller, J. C.; Wade, R. C. *Acc. Chem. Res.* **2016**, *49*, 809−815.
(26) Egwolf, B.; Roux, B. *J. Mol. Biol.* **2010**, *401*, 831−842.
(27) Morais-Cabral, J. H.; Zhou, Y.; MacKinnon, R. *Nature* **2001**, *414*, 37−42.
(28) Ando, H.; Kuno, M.; Shimizu, H.; Muramatsu, I.; Oiki, S. *J. Gen. Physiol.* **2005**, *126*, 529−538.
(29) Iwamoto, M.; Oiki, S. *J. Neurosci.* **2011**, *31*, 12180−12188.
(30) Alcayaga, C.; Cecchi, X.; Alvarez, O.; Latorre, R. *Biophys. J.* **1989**, *55*, 367−371.

(31) Chang, H.-K.; Iwamoto, M.; Oiki, S.; Shieh, R. C. *Sci. Rep.* **2015**, *5*, 18404.

(32) Sumikama, T.; Saito, S.; Ohmine, I. *J. Chem. Phys.* **2013**, *139*, 165106.

(33) Schumaker, M. F.; MacKinnon, R. *Biophys. J.* **1990**, *58*, 975−984.

(34) Roux, B.; MacKinnon, R. *Science* **1999**, *285*, 100−102.

(35) Edman, K.; Nollert, P.; Royant, A.; Belrhali, H.; Pebay-Peyroula, E.; Hajdu, J.; Neutze, R.; Landau, E. M. *Nature* **1999**, *401*, 822−826.

(36) Chung, S.-H.; Allen, T. W.; Hoyles, M.; Kuyucak, S. *Biophys. J.* **1999**, *77*, 2517−2533.

(37) Chandler, D. *Introduction to Modern Statistical Mechanics*; Oxford University Press: New York, 1987.

(38) Rey, R.; Guàrdia, E. *J. Phys. Chem.* **1992**, *96*, 4712−4718.

(39) Kruse, A. C.; Hu, J.; Pan, A. C.; Arlow, D. H.; Rosenbaum, D. M.; Rosemond, E.; Green, H. F.; Liu, T.; Seok, C. P.; Dror, R. O.; Shaw, D. E.; Weis, W. I.; Wess, J.; Kobilka, B. K. *Nature* **2012**, *482*, 552−556.

(40) Yasuda, R.; Noji, H.; Yoshida, M., Jr.; Kinoshita, K.; Itoh, H. *Nature* **2001**, *410*, 898−904.

(41) Kim, H.; Abeysirigunawarden, S. C.; Chen, K.; Mayerle, M.; Ragunathan, K.; Luthey-Schulten, Z.; Ha, T.; Woodson, S. A. *Nature* **2014**, *506*, 334−338.

(42) Oiki, S.; Iwamoto, M.; Sumikama, T. *J. Gen. Physiol.* **2010**, *136*, 363−365.

(43) Oiki, S.; Iwamoto, M.; Sumikama, T. *PLoS One* **2011**, *6*, e16578.

(44) English, B. P.; Min, W.; van Oijen, A. M.; Lee, K. T.; Luo, G.; Sun, H.; Cherayil, B. J.; Kou, S. C.; Xie, X. S. *Nat. Chem. Biol.* **2006**, *2*, 87−94.

(45) MacKinnon, R.; Latorre, R.; Miller, C. *Biochemistry* **1989**, *28*, 8092−8099.

(46) Zhou, Y.; Xia, X.-M.; Lingle, C. J. *Proc. Natl. Acad. Sci. U. S. A.* **2011**, *108*, 12161−12166.

(47) Moscoso, C.; Vergara-Jaque, A.; Márquez-Miranda, V.; Sepúlveda, R. V.; Valencia, I.; Díaz-Franulic, I.; González-Nilo, F.; Naranjo, D. *Biophys. J.* **2012**, *103*, 1198−1207.

(48) Gadsby, D. C.; Bezanilla, F.; Rakowski, R. F.; de Weer, P.; Holmgren, M. *Nat. Commun.* **2012**, *3*, 669.

(49) Berendsen, H. J. C.; Postma, J. P. M.; van Gunsteren, W. F.; DiNola, A.; Haak, J. R. *J. Chem. Phys.* **1984**, *81*, 3684−3690.

(50) Siu, S. W.; Vacha, R.; Jungwirth, P.; Bockmann, R. A. *J. Chem. Phys.* **2008**, *128*, 125103.

(51) Long, S. B.; Campbell, E. B.; MacKinnon, R. *Science* **2005**, *309*, 897−903.

(52) Jorgensen, W. L.; Chandrasekhar, J.; Madura, J. D.; Impey, R. W.; Klein, M. L. *J. Chem. Phys.* **1983**, *79*, 926−935.

(53) Dang, L. X. *J. Am. Chem. Soc.* **1995**, *117*, 6954−6960.

(54) Cornell, W. D.; Cieplak, P.; Bayly, C. I.; Gould, I. R.; Merz, K. M.; Ferguson, D. M.; Spellmeyer, D. C.; Fox, T.; Caldwell, J. W.; Kollman, P. A. *J. Am. Chem. Soc.* **1995**, *117*, 5179−5197.

(55) Berendsen, H. J. C.; Grigera, J. R.; Straatsma, T. P. *J. Phys. Chem.* **1987**, *91*, 6269−6271.

(56) Hornak, V.; Abel, R.; Okur, A.; Strockbine, B.; Roitberg, A.; Simmerling, C. *Proteins: Struct., Funct., Genet.* **2006**, *65*, 712−725.

(57) Essmann, U.; Perera, L.; Berkowitz, M. L.; Darden, T.; Lee, H.; Pedersen, L. G. *J. Chem. Phys.* **1995**, *103*, 8577−8593.

(58) Ryckaert, J. P.; Ciccotti, G.; Berendsen, H. J. C. *J. Comput. Phys.* **1977**, *23*, 327−341.

(59) Case, D. A.; Darden, T.; Cheatham, III, T. E.; Simmerling, C.; Wang, J.; Duke, R. E.; Luo, R.; Walker, R. C.; Zhang, W.; Merz, K. M.; Roberts, B. P.; Hayik, S.; Roitberg, A.; Seabra, G.; Kolossváry, I.; Wong, K. F.; Paesani, F.; Vanicek, J.; Wu, X.; Brozell, S. R.; Steinbrecher, T.; Gohlke, H.; Cai, Q.; Ye, X.; Wang, J.; Hsieh, M.-J.; Hornak, V.; Cui, G.; Roe, D. R.; Mathews, D. H.; Seetin, M. G.; Sagui, C.; Babin, V.; Luchko, T.; Gusaro, S.; Kovalenko, A.; Kollman, P. A. *AMBER 11*; University of California: San Francisco, 2010.

(60) Delemotte, L.; Klein, M. L.; Tarek, M. *Front. Pharmacol.* **2012**, *3*, 97.

(61) Contreras, J. E.; Chen, J.; Lau, A. Y.; Jogini, V.; Roux, B.; Holmgren, M. *Biophys. J.* **2010**, *99*, 2863−2869.

(62) Humphrey, W.; Dalke, A.; Schulten, K. *J. Mol. Graphics* **1996**, *14*, 33−38.